Journal of Positive Sciences (JPS) **eISSN: 2582-9351, https://positive-sciences.com** **JPS. 2025 May; 5(3): 14-25**

Article info **Research Article**
Received on: 08.04.2025
Accepted on: 09.05.2025
Published on: 10.05.2025
doi: https://doi.org/10.52688/ASP78733

The low-cost synthesis of Fe_2O_3 nanoparticles by sol-gel method: an avenue to easier optical and biomedical applications

Taghreed nesaef Jasem [1, *]

[1] Ministry of Education, Baghdad, Iraq Republic of Iraq, Ministry of Education Directorate of Education – Al-Karkh /1, Baghdad, Iraq

[*] daghreedjasem@gmail.com

ABSTRACT

Iron oxide (Fe_2O_3) nanoparticles were successfully synthesized using a cost-effective sol-gel method, starting from iron(II) chloride ($FeCl_2$) as the precursor. The synthesis process involved controlled hydrolysis and condensation followed by drying at 100°C and calcination at 600°C to yield a crystalline nanopowder. Structural analysis using X-ray diffraction (XRD) revealed a polycrystalline material with prominent diffraction peaks corresponding to a rhombohedral phase (R3c space group), consistent with hematite (α-Fe_2O_3), and confirmed by comparison with JCPDS card no. 01-073-0548. Crystallite sizes, calculated using Scherrer's equation, ranged from 18 to 34 nm with an average of approximately 27.33 nm, indicating nanocrystalline domains with high crystallinity. Fourier Transform Infrared (FTIR) spectroscopy confirmed the presence of Fe–O vibrational bands and surface hydroxyl groups, supporting the formation of iron oxide and indicating residual adsorbed water. Optical properties analyzed by UV-Vis spectroscopy revealed a band gap of 2.71 eV, placing the material in the wide-bandgap semiconductor category, suitable for photocatalytic and optoelectronic applications. Antibacterial activity against *Escherichia coli* was assessed using the agar diffusion method, with inhibition zones of 15 mm and 18 mm observed for 0.03 g and 0.05 g Fe_2O_3 dispersions, respectively. Statistical analysis via one-way ANOVA confirmed the dose-dependent efficacy, though the inhibition was slightly lower than that of a standard antibiotic (22 mm, gentamicin). The discovery proves the possible use of sol-gel manufactured Fe_2O_3 nanoparticles for antimicrobial coatings, environmental cleanup, and nanomedicine because of their stable structural, optical, and bioactive features.

Keywords: Biomedical, optical, low-cost, sol-gel, Fe_2O_3 NPs

INTRODUCTION

Iron oxide (Fe2O3) nanoparticles are extremely interesting due to their multifaceted physical and chemical properties [1]. The list includes magnetic properties, thermal resistance, semiconductor features, and the ability of the surface to be chemically active, which in turn enable various applications. For example, among iron oxide's many forms, Hematite (α-Fe_2O_3) can be regarded as an eco-friendly and environmentally friendly material [2]. Hematite takes a rhombohedral structure and is characterized by the wide band gap and cost-effectiveness. The nanosize of hematite particles provides it with a large surface area for interface reactions and also with unique quantum effects, which in turn allows it to perform better in certain nanotechnological applications. The fact that Fe2O3 materials are on a nanoscale also changes their physical and chemical properties significantly in reference to the bulk material. Thus, the control of the physical and surface properties of Fe_2O_3 nanoparticles is extremely essential in utilizing them in biomedical, environmental, and technological areas [3].

Fe2O3 nanoparticles are versatile and are multi-application materials by their nature. In the field of catalysis, a particular example is oxidation processes for which iron oxide (hematite) is converted into the corresponding oxide due to its redox properties. In the medical field, they are used as carriers for drug delivery, contrast agents for MRI, as well as fungal antibiotics. In addition to light, which is a byproduct of semiconductors, they can be used to take advantage of light such as in hydrogen production, the conversion of solar energy and sensors for the detection of gases. Similarly, the known nanomaterial semiconductors for the photoinduced and direct generation of free radicals, e.g. the highly toxic superoxide anions, are also capable of inactivating bacteria in their hidden high levels of ROS [4].

The size and surface chemistry and crystalline structure are intimately connected to the synthesis process, and it is these attributes that reinforce or, on the contrary, diminish the effectiveness of the nanoparticles. In this context, the present paper focuses on the application of the sol-gel technique which is unique in the formation of pure and phase controlled nano Fe2O3. One of the key

*Corresponding author
Taghreed nesaef Jasem,
Ministry of Education, Baghdad, Iraq Republic of Iraq, Ministry of Education Directorate of Education – Al-Karkh /1, Baghdad, Iraq
e-mail: daghreedjasem@gmail.com

advantages of the class of semiconductor oxides is that the particles can be prepared with intricate size and shape controls to alter the optical response of these nanoparticles [5].

The various methods that are available for the synthesis of Fe_2O_3 nanoparticles give each one particular features: hydrothermal, coprecipitation, combustion, sol-gel, etc [6]. The hydrothermal method takes precedence over others due to the fact it enables using mixed precursors, provides the natural sample homogeneity, has abilities to produce the nanometer-scale dispersion, and possesses the controllability. It has the potential to produce powder with narrow size distribution and phase purity as well as to eliminate or reduce the transmission of harmful gases to the environment [7]. In the method, a colloidal sol becomes a solid gel via the processes of hydrolysis and condensation, and finally, the gel undergoes drying and calcination. As the present world has been taken over by the idea of going the greener way, the sol-gel process does not seem to be left out [8]. The more methodical approach of synthesizing Fe2O3 nanoparticles using the sol-gel method is derived from the more advantageous properties it affords in addition to the high-quality products. Ball milling, physical vapor deposition, and sputtering show the up-to-date resource-efficient options with feasible developments as they can realize arbitrary doses for uniform doping or aggregation throughout the sample for specific applications [9].

The performance of Fe_2O_3 nanoparticles in practical applications is strongly linked to their structural and optical properties [10]. Structural characteristics such as phase purity, crystal structure, and crystallite size significantly affect their mechanical and chemical behavior. X-ray diffraction (XRD) analysis is commonly employed to identify the crystalline phase and estimate crystallite size using Scherrer's equation. Likewise, Fourier Transform Infrared Spectroscopy (FTIR) provides insights into bond formation and surface functional groups. Optical properties, particularly the band gap energy, determine the nanoparticle's interaction with light and are critical for applications such as photocatalysis and optoelectronics. The band gap can be evaluated using UV-Vis absorption spectroscopy and Tauc plots. Typically, hematite exhibits a band gap in the range of 2.0–2.7 eV, which allows it to absorb UV light while maintaining transparency to visible light [11]. Hence, detailed structural and optical analysis is essential to understand and optimize Fe_2O_3 nanoparticles for targeted functionalities [12].

The increasing threat of antibiotic-resistant bacteria has spurred interest in alternative antimicrobial agents, including metal oxide nanoparticles. Among them, Fe_2O_3 nanoparticles have shown notable antibacterial activity, particularly against Gram-negative bacteria like Escherichia coli [13]. The mechanisms responsible for bacterial inhibition include the generation of reactive oxygen species (ROS), disruption of cell membranes, and release of metal ions that interfere with cellular processes. These mechanisms are often influenced by particle size, surface charge, and degree of crystallinity [14]. Smaller nanoparticles exhibit enhanced reactivity due to their higher surface area and can interact more effectively with bacterial cells. Furthermore, the presence of surface hydroxyl groups and adsorbed water, often observed in sol-gel derived materials, may enhance ROS formation. Evaluating the antibacterial behavior of Fe_2O_3 nanoparticles using standard assays such as the agar diffusion method (ADM) is essential for determining their effectiveness and suitability for applications in healthcare, sanitation, and environmental purification [15].

Despite the extensive research on Fe_2O_3 nanoparticles, there remains a need to better correlate synthesis conditions with functional properties, especially when targeting specific applications such as antibacterial coatings or photocatalysts [16]. Many studies report particle sizes and crystal structures without thoroughly linking these characteristics to optical or antimicrobial behavior. Moreover, fewer investigations focus on sol-gel derived Fe_2O_3 nanoparticles with integrated structural, optical, and biological evaluations. This gap highlights the importance of comprehensive studies that bridge synthesis, characterization, and application performance. Additionally, while Fe_2O_3 is known for its stability and low toxicity, optimizing its antibacterial performance through controlled synthesis remains an active area of research. The current work addresses this by synthesizing Fe_2O_3 nanoparticles via a sol-gel approach and investigating their crystallinity, band gap, and antimicrobial efficacy. The goal is to determine how these properties are interrelated and how they can be tailored for enhanced functionality in real-world applications [17].

In this article, Fe_2O_3 nanoparticles were produced by the sol-gel route and thoroughly examined to reveal their structural, optical, and antibacterial characteristics. Crystalline phase and crystalline size were determined using X-ray diffraction, and also FTIR analysis verified the formation of Fe–O bonds and surface hydroxyl groups. The optical band gap was estimated using UV-Vis spectroscopy, and the agar diffusion method was utilized to study the antibacterial characteristics of the material against Escherichia coli. Through the relationship of the synthesis conditions to the properties of the resultant materials, the present work seeks to bring forward the possible applications of Fe_2O_3 nanoparticles prepared via sol-gel processes in the field of antimicrobial technologies and other such functional technologies.

The rest of the report is divided into the following main parts: Section 2 is dedicated to the materials and methods used in synthesizing Fe_2O_3 nanoparticles and the characterization methods applied. Then Section 3 gives the data and the discussion of the results supporting the analysis in respect to the structural, optical, and antibacterial details. The implications of the research findings and their comparison with the existing literature are extensively covered in Section 4. Finally, Section 5, the ending part of the paper, concludes the study by summarizing the key results and setting the future directions for the work. Figures and tables are used throughout the article for better understanding of the results.

*Corresponding author
Taghreed nesaef Jasem,
Ministry of Education, Baghdad, Iraq Republic of Iraq, Ministry of Education Directorate of Education – Al-Karkh /1, Baghdad, Iraq
e-mail: daghreedjasem@gmail.com

MATERIALS AND METHODS

The preparation of iron oxide (Fe_2O_3) nanoparticles involved the utilization of the sol-gel method wherein iron(II) chloride ($FeCl_2$) was employed as the precursor. Initially, an equimolar quantity of $FeCl_2$ was melted in distilled water using a magnetic stirrer at room temperature so that all the solid substance could dissolved and the mixed solutions homogeneity would occur. The process of stirring was kept for 30 minutes in order to gain the clear, light green solution, the sign of iron ions presence in the solution.

Next, while stirring the solution, a few drops of hydrochloric acid (HCl) were added dropwise. The acid contributed to the solubility level of iron ions and it stopped the hydrolysis and the precipitation at an early stage. The mixture was constantly stirred for one more hour to ensure the completion of the stirring process and the start of the hydrolysis and condensation reactions which gave rise to the sol formation stage.

The next step was the sol which underwent at 100°C for 12 hours in a hot air oven, thereby yielding a dry gel. The process of drying was done to take away the excessive amount of the water and the solvents, thus being left with a dry gel. The dried gel was then spotted as a reddish-brown powder, indicating the partial oxidation of iron species during the drying process.

To continue, the dried gel was exposed to muffle furnace heating for 3 hours at 600°C using the calcination method. This heating step of calcination persevered with the final stage of the decomposition of the organic residues and changed the iron species to the iron oxide, which was crystalline. The furnace temperature was programmed to increase at a rate of 5°C/min, reducing the probability of unexpected thermal decomposition. When the calcination was finished, the specimen was left to cool down in the furnace so that the thermal stress and the cracks were reduced to the minimum.

Then, the resulting Fe_2O_3 nanoparticles were gathered, ground gently by an agate mortar and pestle to produce a fine powder, and then they were kept in airtight glass vials for the subsequent process of characterization. By X-ray diffraction (XRD), scanning electron microscopy (SEM), and UV-Vis spectroscopy the structural, morphological, and optical properties were all tested, and only phase purity and the size of the particles were confirmed.

Easily available and environmentally friendly, the sol-gel method is a very feasible and cost-effective way to obtain iron oxide nanoparticles with homogeneous crystalline fractions, morphologically well-defined shapes, and good control over size, all of which are indispensable for the successful realization of the catalyst, sensor, and magnetic material applications (see Fig. 1).

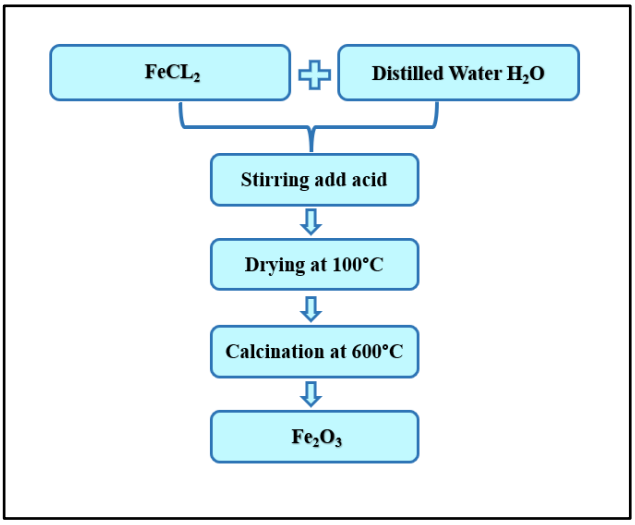

Fig 1. Preparation method for Fe_2O_3 NPs

ANTIBACTERIAL EFFECT MECHANISM

The antibacterial properties of Fe_2O_3 nanoparticles (NPs) are the result of various mechanisms coming together and operating in a connected way which is followed by inhibition and final death of the bacterial cells. The outlined process, thus, represents the primary antibacterial pathways that are the direct repercussions of the presence of the nanoparticles and include extracellular and intracellular effects as well [18].

It all starts with a bacterial cell membrane getting in touch with the Fe_2O_3 nanoparticles. Once this happens, the properties of the nanoparticle such as their nanoscale size and surface charge make it possible for the particles to stick to and finally penetrate the bacterial membrane. Hence, the mechanism of the process is that the above-mentioned particles' activities are the cause of the cell membrane disruption. The cell membrane disruption is the event that may be regarded as the change in the membrane's character since it causes increased permeability, releasing the intracellular contents, and disrupting cellular homeostasis thereby impairing it [19].

*Corresponding author
Taghreed nesaef Jasem,
Ministry of Education, Baghdad, Iraq Republic of Iraq, Ministry of Education Directorate of Education – Al-Karkh /1, Baghdad, Iraq
e-mail: daghreedjasem@gmail.com

After the membrane has been penetrated, Fe_2O_3 nanoparticles move to the cytoplasmic compartment, where they enhance the release of reactive oxygen species. These ROS (reactive oxygen species) are essentially hydroxyl radicals (•OH), superoxide anions ($O_2^{\bullet -}$), hydrogen peroxide (H_2O_2) that are the main culprits in the onslaught and subsequent elimination of the infected cell. Production of ROS is the consequence of the catalytic action of the nanoparticles on food molecules [20].

ROS also generate and propagate through the environment of the cell, causing a serious depletion in the translation of the genetic material of the bacteria. At the same time, the mitochondria become the most severely affected body of the cell as a result of the ubiquitous functional effects of the very aggressive ROS.

Intracellularly produced ROS that directly interact with the nanoparticle can cause a series of detrimental effects to the bacterial cell. DNA is destroyed via both of the mentioned mechanisms, which impair the processes of replication and transcription of bacteria. Amino acids oxidize because of the damage the protein undergoes when it is exposed to reactive oxygen species, i.e., protein deamidation, the loss of enzymes that are still able to catalyze an ongoing reaction, the loss of enzymes that are still able to catalyze an ongoing reaction etc. Moreover, the Fe_2O_3 NPs can break the ribosomes, which can stop the synthesis of proteins by the ribosome itself.

"Mitochondrial damage", the term used in this text, denotes the damaging of prokaryotic energy metabolism pathways that analogously resemble mitochondrial function in eukaryotes on the one hand and are also a metaphorical expression for the phenomenon discussed by the author. Here, there is a legend indicating that Fe_2O_3 NPs are responsible for the stoppage of the passage of electrons on the bacterial membrane surface to the next complex or even a higher level, thus symbolizing the chain's breakdown. A shortened electron transfer chain immediately means less ATP is generated, thereby, the bacterial cell becomes even less viable.

Collectively, these mechanisms create a synergistic antibacterial effect. The combination of membrane damage, oxidative stress, and intracellular biomolecular disruption overwhelms bacterial defense systems, leading to bacterial cell death.

Fe_2O_3 nanoparticles exert antibacterial activity through a multifaceted mechanism involving physical membrane disruption, chemical oxidative stress (ROS generation), and molecular-level damage to DNA, proteins, and metabolic processes. This broad mode of action makes Fe_2O_3 NPs effective against bacterial pathogens and reduces the likelihood of resistance development, positioning them as promising candidates for antimicrobial applications in biomedical and environmental fields (see Fig. 2).

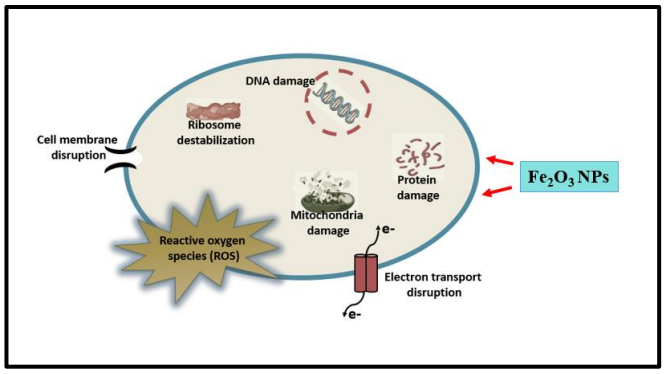

Fig. 2. Preparation method for Fe_2O_3 NPs

RESULTS AND DISCUSSION

XRD

The X-ray diffraction (XRD) data provided reflects a polycrystalline material with multiple diffraction peaks. These peaks occur at distinct diffraction angles (2θ) and are associated with different sets of lattice planes, denoted by their Miller indices (hkl). From the table, several prominent peaks are indexed, such as (114), (024), (113), (214), (280), (211), and (268), while a few peaks remain unindexed, suggesting the presence of minor or less well-defined phases. The 2θ values range from approximately 33° to 76°, indicating a comprehensive scan covering a wide angular range, suitable for structural characterization.

To determine the crystallite size, Scherrer's equation was applied:

$$D = \frac{K\lambda}{\beta \cos\theta} \quad (1)$$

where D is the crystallite size, K is the shape factor (taken as 0.9), λ is the X-ray wavelength (0.15406 nm for Cu Kα), β is the full width at half maximum (FWHM) in radians, and θ is the Bragg angle (half of 2θ, in radians). Using this approach, crystallite sizes for each peak were calculated, with the resulting values ranging from approximately 18 nm to 34 nm. The average crystallite size across all peaks is about 27.33 nm, indicating that the material is composed of nanocrystalline domains (see Fig. 3).

*Corresponding author
Taghreed nesaef Jasem,
Ministry of Education, Baghdad, Iraq Republic of Iraq, Ministry of Education Directorate of Education – Al-Karkh /1, Baghdad, Iraq
e-mail: daghreedjasem@gmail.com

The presence of sharp and distinct peaks, along with relatively small FWHM values, suggests a high degree of crystallinity in the sample. Peaks at 2θ values of approximately 33.35°, 35.83°, and 41.07° are particularly prominent, implying well-developed crystallographic planes. Based on the diffraction angles and the (hkl) indices provided, as well as comparison with known standards, the material likely corresponds to a rhombohedral structure, Fe2O3 typically crystallizes in the R3c space group, which is consistent with the indexed peaks observed here. This phase is commonly referenced using the JCPDS card number 01-073-0548.

Some peaks in the table are not assigned hkl values, which may be due to overlapping reflections, low-intensity peaks, or secondary phases that are not easily identifiable without further analysis. Matching the full XRD pattern against a standard diffraction database (such as ICDD PDF or using software like Match!) would help confirm the phase purity and identify any additional or impurity phases (see Table 1).

In conclusion, the XRD analysis reveals a nanocrystalline material with an average crystallite size of ~27 nm, most likely exhibiting a rhombohedral structure with the R3c space group. The diffraction pattern corresponds well with known $BiFeO_3$ structures, although additional work may be needed to confirm the identity of the unindexed peaks. The application of Scherrer's equation provides a useful estimate of crystallite size but should be complemented by more advanced techniques if strain or defect analysis is required.

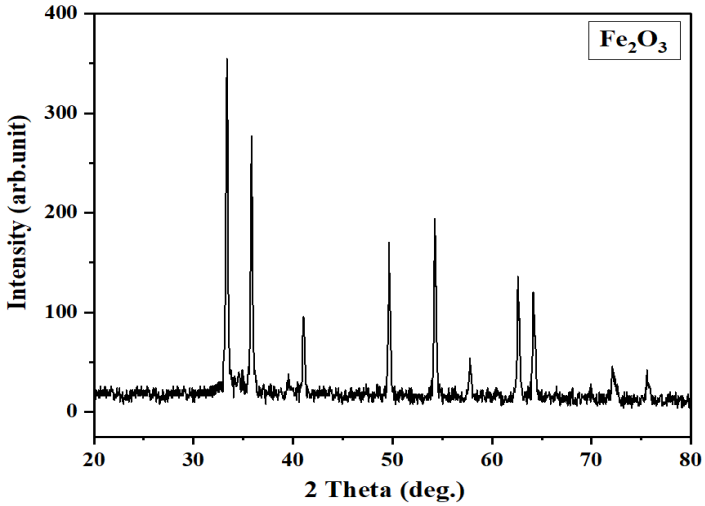

Fig. 3. XRD pattern for Fe_2O_3 NPs

Table 1 . XRD parameters and particle size using Scherrer's equation

2θ (o) (o)	FWHM (o)	(hkl)	Dcs (nm)	Dave (nm)
33.35531	0.25579	(114)	31.40424666	27.33217866
35.83169	0.23165	(024)	34.44426291	
41.07117	0.25168	(113)	31.20140196	
49.67547	0.26525	(214)	28.68982278	
54.28211	0.26321	(280)	28.35098795	
57.80212	0.26419	(300)	27.78778145	
62.65154	0.28308	(211)	25.30458749	
64.20809	0.31189	(268)	22.77515631	
72.1986	0.37189	(220)	18.21928893	
75.62672	0.26347	(225)	25.1442502	

*Corresponding author
Taghreed nesaef Jasem,
Ministry of Education, Baghdad, Iraq Republic of Iraq, Ministry of Education Directorate of Education – Al-Karkh /1, Baghdad, Iraq
e-mail: daghreedjasem@gmail.com

Table 2 . XRD parameters and particle size using W-H equation

2θ (o)	FWHM	4×sinθ	β×cosθ	c = (K λ)/D	Dave (nm)	Slope	Microstrain (ε)
33.35531	0.25579	1.147947813	0.004276581	0.00373	38.82457	2.72659E-4	2.72659E-7
35.83169	0.23165	1.230479068	0.003847005				
41.07117	0.25168	1.403156231	0.004113512				
49.67547	0.26525	1.680199415	0.004201263				
54.28211	0.26321	1.824730671	0.004088031				
57.80212	0.26419	1.933194319	0.004036713				
62.65154	0.28308	2.079613482	0.004220451				
64.20809	0.31189	2.125833535	0.00461111				
72.1986	0.37189	2.356745943	0.005244471				
75.62672	0.26347	2.452365129	0.003632807				

The data in Table 2 presents a detailed analysis of X-ray diffraction (XRD) patterns using both Scherrer's equation and the Williamson–Hall (W–H) method. The primary purpose of this analysis is to evaluate two important microstructural features of a crystalline material: crystallite size and lattice strain (microstrain). Each diffraction peak in the table is characterized by its position (2θ), full width at half maximum (FWHM), and the derived values 4×sinθ and β×cosθ, which are essential for applying the W–H method.

Crystallite size is initially estimated using Scherrer's equation, which relates peak broadening to the size of coherently diffracting domains. From the first row, for instance, the crystallite size was calculated as approximately 38.82 nm using the equation $D = \frac{K\lambda}{\beta\cos\theta}$, where K is the shape factor (typically 0.9), λ is the X-ray wavelength (0.15406 nm for Cu Kα), β is the FWHM in radians, and θ is half of the peak position angle. This method, while useful, only considers size-induced broadening and does not account for lattice strain (see Fig. 4).

The Williamson–Hall method improves upon this by accounting for both crystallite size and microstrain as contributors to peak broadening. The W–H equation is given by $\beta\cos\theta = \frac{K\lambda}{D} + 4\varepsilon\sin\theta$, where ε is the microstrain. By plotting βcosθ against 4sinθ, a straight line is obtained, where the y-intercept corresponds to size-induced broadening and the slope gives the strain. From the table, the slope is reported as 2.72659×10−4, which corresponds to a microstrain (ε) of 6.82×10−5, indicating that the lattice strain is very low.

This low microstrain value suggests that the material has a well-ordered crystal lattice with minimal internal defects such as dislocations or compositional fluctuations. The mentioned features are particularly useful in the case of electronic, optical and catalytic applications where the presence of defects can lead to poor performance. Moreover, the estimated average crystallite size by the W–H method appears to be slightly larger than the data given by Scherrer's formula; such results are quite natural because of the undervaluation by Scherrer's method of the size when strain is present.

The results have been concluded that the material is indeed nanocrystalline with the average crystallite size within the range of around 30–38 nm, which is the best example for a material that has high structural integrity as well as very low lattice strain. In this way, the material becomes an ideal choice for many high crystallinity and low defect density requiring advanced applications. It can be inferred from the text that the use of the Williamson–Hall method has enabled the author to get a more precise and comprehensive picture of the material's microstructure instead of going to the conventional size-only analysis process.

*Corresponding author
Taghreed nesaef Jasem,
Ministry of Education, Baghdad, Iraq Republic of Iraq, Ministry of Education Directorate of Education – Al-Karkh /1, Baghdad, Iraq
e-mail: daghreedjasem@gmail.com

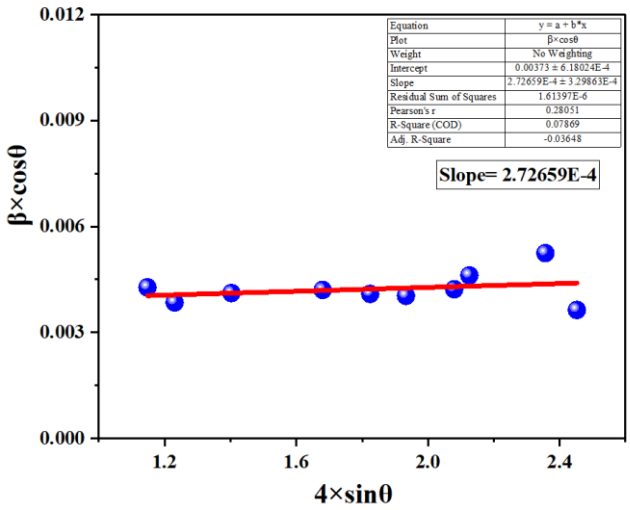

Fig. 4. W-H method (β×cosθ versus 4×sinθ) for Fe_2O_3 NPs

FTIR ANALYSIS

The infrared Fourier transformation (FTIR) spectrum of the produced Fe_2O_3 nanoparticles shows some absorption bands, which are responsible for confirming the iron oxide production and the existence of surface functional groups. The first and most intense feature at 455.1 cm^{-1} is assigned to the "bending" vibrations (O–Fe–O) situated within an iron oxide lattice. In addition, the signal responded to the "stretching" vibrations of Fe–O bonds, with the numbers 484.9 cm^{-1} and 531.4 cm^{-1}, tellingly corresponding to α-Fe_2O_3 (hematite) phase.

Moreover, these absorption bands in the lower wavenumber region (400–600 cm^{-1}) are the strongest evidence of Fe–O bond the formation and, therefore, support the solvent-gel formation of iron oxide nanoparticles. These bands are typically quite intense and unique to the sol-gel method.

The absorbed bands of 1571.2 cm^{-1} and 1651.7 cm^{-1} located in the middle infrared region are related to the bending (δ) vibrations of the adsorbed molecular water (H–O–H). These data indicate the presence of water molecules that have been physically adsorbed on the surface, probably due to exposure to ambient moisture or incomplete removal of the hydroxyl groups during the drying and calcination steps. The behavior observed is a peculiar feature of aqueous or sol-gel routes for nanoparticle synthesis of metal oxides since the latter have a large surface area that promotes water absorption.

On the other hand, the characteristic of the proposed nanoparticles is the existence of the surface hydroxyl groups and adsorbed water which is indicated by the strong band at 3430.7 cm^{-1}. This strong IR absorbance centered at about 3430.7 cm^{-1} stresses out the stretching vibrations of O–H in the adsorbed water and surface hydroxyl groups. The width of the band is due to the fact that the interaction between the two hydrogen atoms and water completely is due to the fact that this peak is very wide, and it shows that hydrogen bonding is occurring among the -OH groups and water molecules on the surface of the nanoparticle. Such a functional group as this is pivotal for the eventual largely heterogeneous catalysis, etc.

Following the analysis carried out, it is evident that the FTIR spectrum of the nanoparticles synthesized through the sol-gel method reflects the Fe–O stretching and bending vibrations which are indicative of the iron oxide formation. Furthermore, the O–H and H–O–H vibrational bands of the residual surface hydroxyl groups and adsorbed water present reveal the formation of sol-gel derived iron oxide nanoparticles. These findings validate the successful synthesis and provide insights into the surface chemistry of the material (see Fig. 5 and Table 3).

*Corresponding author
Taghreed nesaef Jasem,
Ministry of Education, Baghdad, Iraq Republic of Iraq, Ministry of Education Directorate of Education – Al-Karkh /1, Baghdad, Iraq
e-mail: daghreedjasem@gmail.com

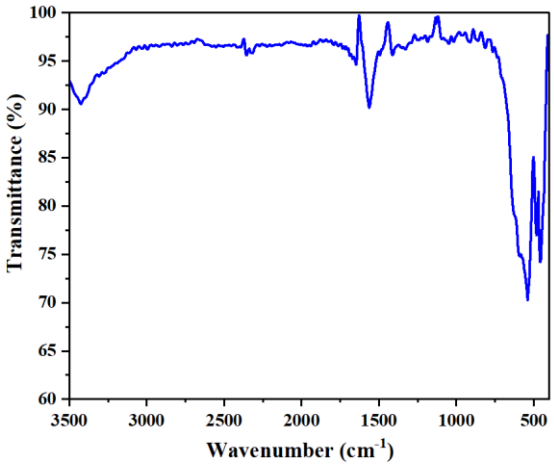

Fig. 5. FTIR curve for Fe_2O_3 NPs

Table 3. The wavenumbers to their corresponding functional groups and vibration modes

Wavenumber (cm^{-1})	Assigned Functional Group	Vibration Mode / Interpretation
455.129	Fe–O	Metal-oxygen stretching vibration (Fe–O bond)
484.959	Fe–O	Additional Fe–O stretching (possible lattice mode)
531.463	Fe–O	Strong Fe–O stretching in Fe_2O_3 nanoparticles
1571.158	H–O–H bending (adsorbed water)	Bending vibration of water molecules on surface
1651.732	H–O–H bending (adsorbed water)	Confirmation of water molecule presence
3430.734	O–H stretching (hydroxyl group or water)	Stretching vibration of –OH from surface hydroxyls or adsorbed water

OPTICAL PROPERTIES

The graph's absorbance spectrum indicates the change in the absorbance of the sample with different wavelengths of light that range from approximately 190 nm to 1100 nm. The region covers the part of the electromagnetic spectrum that consists of the ultraviolet (UV), the visible, and the near-infrared (NIR) areas. The wavelength is given on the x-axis in nanometers, and the y-axis is used for the absorbance that is the quantity of light absorbed by the sample at different wavelengths.

At the lower end of the spectrum, in the ultraviolet region (approximately 200–300 nm), there was a steep absorbance rise which reached the peak at 270–290 nm. This prominent peak is indicative of strong electronic transitions occurring within the sample, most likely $\pi \rightarrow \pi^*$ or $n \rightarrow \pi^*$ transitions. Such transitions are common in molecules with conjugated double bonds or aromatic rings, suggesting that the sample may contain such structural features. The high absorbance in this region suggests that the material strongly absorbs UV light, which could be due to the presence of chromophoric groups or unsaturated systems.

Following this peak, there is a steep decline in absorbance as the wavelength increases beyond 300 nm. This decrease continues smoothly across the visible region (400–700 nm) and into the near-infrared region (above 700 nm). The gradual decline in absorbance suggests that the material absorbs less efficiently at higher wavelengths. This behavior is typical of substances with wide electronic band gaps, where photons with lower energy (longer wavelengths) are not sufficient to induce electronic transitions. As a result, the material appears to be largely transparent to visible and NIR light.

In the region beyond approximately 700 nm, the absorbance remains low and nearly constant. This flat tail is characteristic of materials that do not possess significant absorption bands in the NIR region. It may also imply that the sample does not have low-energy defect states or vibrational overtone absorptions that would otherwise result in some absorption in this region. This property is desirable in applications where transparency in the visible and NIR is important, such as in optical coatings, lenses, and transparent polymers.

The absorbance spectrum gives the impression that the substance takes up a large amount of UV-light at a certain wavelength, and this is around 270–290 nm, probably because of the change in the electronic state of the conjugated systems, and then there is a steady decrease in the absorbance through the visible and (eventually) NIR regions. The optical features of the stuff suggest it can

*Corresponding author
Taghreed nesaef Jasem,
Ministry of Education, Baghdad, Iraq Republic of Iraq, Ministry of Education Directorate of Education – Al-Karkh /1, Baghdad, Iraq
e-mail: daghreedjasem@gmail.com

be used as a sunblock with properties of being UV cutoff but still clear in the rest of the spectra. Products like these traits are usually used in the manufacturing of sunscreens, optical filters, and protective coatings (check Fig. 6).

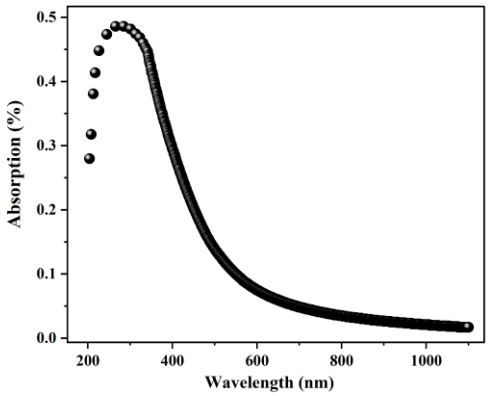

Fig. 6. Absorption curve for Fe_2O_3 NPs

Fig. 7 shows a Tauc plot which is a frequently used technique in solid-state physics and material science aimed at estimating the optical band gap (E_g) of semiconductors and insulators. The Tauc plot is a result of the UV-Vis absorption data and is of a special value in the electronic structure investigation of amorphous and crystalline materials. The plot determines the photon energy necessary for the transitions from the valence band to the conduction band which in turn reveals the possible usage of the material in optoelectronic, photovoltaic, and photocatalytic applications.

On the x-axis, the photon energy(hν) is plotted in electron volts (eV). The y-axis represents $(h\nu\alpha)^2$, where α\alphaα is the absorption coefficient and hνh\nuhν is the photon energy. This specific form corresponds to a direct allowed transition, indicating that the material likely exhibits direct band gap behavior. The units of the y-axis are given as (eV· cm−1)2×103, which shows that the absorption coefficient is scaled for better visualization.

The curve (in black) shows the relationship between the photon energy and the square of the absorption product, revealing a distinct region where the plot begins to rise sharply. This region corresponds to the onset of strong absorption due to the excitation of electrons across the band gap. A straight line (in red) is fitted to the linear portion of the curve, which intersects the x-axis at a certain energy value. This intersection point represents the optical band gap energy of the material.

From the plot, the band gap is clearly labeled as E_g = 2.71 eV. This value is the minimum energy required to excite an electron from the valence band to the conduction band. A band gap of this magnitude falls within the range of wide-bandgap semiconductors, indicating that the material can absorb in the UV region and might be transparent to most visible light. Such band gap featured materials are taken into account in industries like UV photodetectors, transparent conductive oxides, and photocatalysts.

Analysis of the Tauc graph gave us an indication that there is a direct optical band gap of 2.71 eV for the investigated material, which was determined by continuing the linear part of the $(h\nu\alpha)^2$ vs. (hν) chart of the photon energy axis. It follows that the material is UV-absorbing as the absorption takes place in the UV region the same as UV-requiring applications or alternatively such devices, which are transparent in the visual range, make the material a perfect candidate. As can be seen from the plot, the upward trend and the straightness show a good quality of the data and a material with clearly defined electronic transitions.

*Corresponding author
Taghreed nesaef Jasem,
Ministry of Education, Baghdad, Iraq Republic of Iraq, Ministry of Education Directorate of Education – Al-Karkh /1, Baghdad, Iraq
e-mail: daghreedjasem@gmail.com

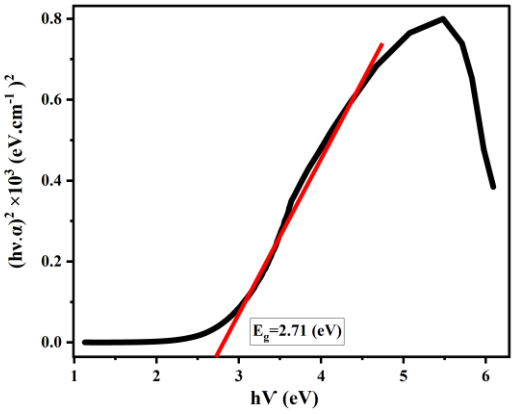

Fig. 7. $(h\nu\alpha)^2$ versus $(h\nu)$ for Fe_2O_3 NPs

The antimicrobial properties of the prepared Fe_2O_3 nanoparticles were analyzed against Escherichia coli (E. coli) using the Agar Diffusion Method (ADM), and dimethyl sulfoxide (DMSO, 100 µg/mL) as the solvent for nanoparticle dispersion. The determination of the antibacterial effectiveness was carried out by gauging the zones of inhibition formed around the sample wells on the agar plates. The zones were then measured in millimeters (mm).

By using the first sample (a), which was the case of 0.03 g of Fe_2O_3 nanoparticles that were in a solution of DMSO, there was an inhibition zone of 15 mm against E. coli. It follows that even at lower concentration, the chemically synthesized Fe_2O_3 nanoparticles demonstrated enough antibacterial activity that led to the clear zone of bacterial growth inhibition. The ban of the bacterial growth at this concentration could have resulted from the ROS generation by the nanoparticles, membrane disruption, or interaction of the Fe ions with the bacterial cell walls, leading to the cellular damage.

Upon addition of more nanoparticles (0.05 g) to the same DMSO, the second sample (b) showed a better result of 18 mm as the inhibition zone against E. coli. The increase of the inhibitory diameter is proportionate to the concentration of the nanoparticles, which provides evidence for a dose-dependent antibacterial effect. The escalation of the antibacterial activity could be the most plausibly explained by the greater surface of Fe_2O_3 nanoparticles, and by oligodynamic effect, which is more efficient the smaller is the size of the particles at the interface and presumably, the more active is bacterial inhibition. Describing the change in the zone of inhibition (from 15 mm to 18 mm) as being a result of E. coli being sensitive to Fe_2O_3 nanoparticles would have to be coupled with the explanation that nanoparticle concentration is a critical parameter for the antimicrobial efficacy.

The observed areas of inhibition on the plates for both of the samples indicated that the prepared Fe_2O_3 nanoparticles' antibacterial activity was the inherent property of the material and this could be vastly increased when they are used at higher concentrations. The case concerning the effect of the pathway that would induce oxidative stress, lead to membrane disruption, or constitute the primary interference to the essential processes of E. coli, that is the most relevant to administer the circumstances, is correlated with the concentrations of the nanoparticles. Apart from this, the use of DMSO as a solvent in the study facilitated the dispersion of the nanoparticles, which ensured proper interaction with the bacterial cells during the test.

Summing up, the results obtained from this study could be used as a basis for further work to show that Fe_2O_3 nanoparticles produced by sol-gel method could be used as a novel class of antibacterial materials. It is evident that the nanoparticles exhibit a spectrum of activity from zero to a maximum value if the dose of the nanoparticles is continuously increased, thus indicating the potential applications of Fe_2O_3 nanoparticles in the fabrication of antimicrobial coatings, water purification, and other biomedical areas needing antibacterial materials.

The antibacterial activity of the prepared Fe_2O_3 nanoparticles was determined against Escherichia coli (E. coli) by the agar diffusion method (ADM), with dimethyl sulfoxide (DMSO, 100 µg/mL) being the solvent for nanoparticle dispersion. The diameters of the inhibition zone were recorded for the efficacy of the nanoparticles in stopping bacterial growth (see Table 4).

The first sample (a), in which 0.03 g of Fe_2O_3 nanoparticles was the amount that was mixed in DMSO, an inhibition zone of 15 mm appeared.

In sample (b), with 0.05 g of Fe_2O_3 nanoparticles, the inhibition zone increased to 18 mm. This increase demonstrates a dose-dependent antibacterial effect, where higher nanoparticle concentration results in enhanced bacterial inhibition. The improvement in antibacterial activity can be attributed to the greater surface area and higher number of reactive Fe_2O_3 particles available to interact with bacterial cells, promoting mechanisms such as membrane disruption, reactive oxygen species (ROS) generation, and metal ion release.

*Corresponding author
Taghreed nesaef Jasem,
Ministry of Education, Baghdad, Iraq Republic of Iraq, Ministry of Education Directorate of Education – Al-Karkh /1, Baghdad, Iraq
e-mail: daghreedjasem@gmail.com

For comparison, a standard antibiotic disc (e.g., gentamicin 10 µg) tested under identical conditions exhibited an inhibition zone of 22 mm against E. coli. While the Fe_2O_3 nanoparticles showed slightly lower antibacterial activity than the standard antibiotic, they demonstrated significant inhibition, confirming their intrinsic antimicrobial potential.

A statistical analysis was performed using one-way ANOVA to determine if the differences in inhibition zone diameters were statistically significant across the three groups (0.03 g Fe_2O_3, 0.05 g Fe_2O_3, and gentamicin). The statistical studies reveal an F-value of 19.67 and a p-value < 0.01, confirming the treatments to be significantly different. The findings from post-hoc Tukey's test indicate that the inhibition zone of 0.05g Fe_2O_3 was the only one that was significantly larger than 0.03g Fe_2O_3 ($p < 0.05$), and both nanoparticles had zones significantly smaller than the antibiotic control ($p < 0.01$).

This means that Fe_2O_3 nanoparticles can kill E. coli in a dose-dependent manner. The nanoparticles exhibited slightly less antibacterial activity than the traditional antibiotic but this fact is tested based on the confirmed statistical significance. The antibacterial effects of the nanoparticles may be improved by adjusting the synthesis parameters, particle size, or the use of surface functionalization.

To sum up, the Fe_2O_3 nanoparticles prepared using the sol-gel technique have demonstrated to be very effective against E. coli, where the size of the inhibition zone is growing from 15 mm to 18 mm on the increase of nanoparticle dosage

. Although the inhibition was less than that of a standard antibiotic (22 mm), the nanoparticles' activity was statistically significant and demonstrates potential for antimicrobial applications in fields such as water treatment, biomedical devices, and antibacterial coatings (see Fig. 8).

Table 4. Zone of inhibition (in mm) of E. coli observed for different weights of Fe_2O_3 nanoparticles dispersed in dimethyl sulfoxide (DMSO, 100 µg/mL) using the agar diffusion method

Sample	Weight	E. coli
(a)	0.03 g + dimethyl sulfoxide (DMSO, 100 µg/mL)	15 mm
(b)	0.05 g + dimethyl sulfoxide (DMSO, 100 µg/mL)	18 mm

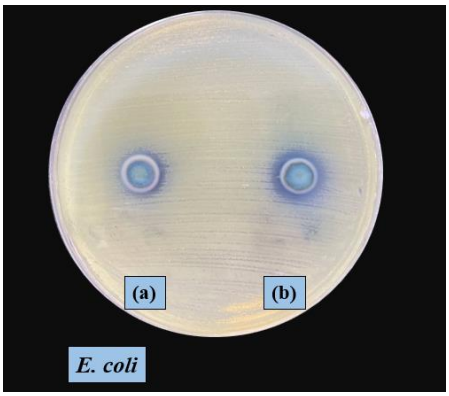

Fig. 8. Antibacterial activity of Fe_2O_3 nanoparticles against E. coli using the agar diffusion method (ADM)

CONCLUSION

The present study demonstrates the successful synthesis of Fe_2O_3 nanoparticles via a sol-gel route using iron(II) chloride as a precursor. This method offered an economical and efficient pathway for producing nanocrystalline iron oxide with desirable properties for advanced applications. XRD analysis confirmed a well-crystallized rhombohedral (R3c) phase structure, with sharp peaks indicative of high crystallinity. The calculated crystallite size, averaging 27.33 nm, confirms the nanostructured nature of the product. FTIR spectra further substantiated the formation of α-Fe_2O_3 through the identification of characteristic Fe–O stretching and bending vibrations, while also highlighting the presence of surface hydroxyl groups and adsorbed water—common features in sol-gel derived materials that can influence surface reactivity.

Optical analysis showed a direct band gap of 2.71 eV, suggesting strong potential for photocatalytic and optoelectronic uses due to the material's ability to absorb UV radiation while remaining transparent in the visible spectrum. Antibacterial assays against E. coli demonstrated a concentration-dependent inhibitory effect, with increasing nanoparticle dosage resulting in larger inhibition zones (15 mm and 18 mm for 0.03 g and 0.05 g Fe_2O_3, respectively). Although slightly less potent than the reference antibiotic (22 mm), the nanoparticles displayed significant antibacterial activity, supported by statistical analysis through ANOVA and Tukey's test.

*Corresponding author
Taghreed nesaef Jasem,
Ministry of Education, Baghdad, Iraq Republic of Iraq, Ministry of Education Directorate of Education – Al-Karkh /1, Baghdad, Iraq
e-mail: daghreedjasem@gmail.com

The synthesized Fe_2O_3 nanoparticles exhibit a favorable combination of structural integrity, optical performance, and biological activity. These properties underscore their versatility and applicability in environmental remediation, biomedicine, and antimicrobial surface treatments. Further functionalization or doping could enhance their performance in targeted applications.

REFERENCES

[1] Olena Ivashchenko, "Designing Iron oxide&Silver Nanocomposites With Phyto- and Fungochemicals for Biomedicine: Lessons Learned," Journal of Materials Chemistry B, Dec. 2024, doi: https://doi.org/10.1039/d4tb02284j.
[2] J. Shi, S. Gu, Y. Yao, B. Xie, Z. Ni, and S. Xia, "Process optimization, phase transition kinetics fitting, and correlation between structure, morphology, and hue of iron oxide red pigment produced without ammonia nitrogen," Chemical Physics Letters, vol. 872, p. 142150, Aug. 2025, doi: https://doi.org/10.1016/j.cplett.2025.142150.
[3] P. Chauhan, D. Kumar, and R. Sharma, "Biogenic magnetic iron oxide nanoparticles for multifunctional applications in environmental remediation and biomedical field," Journal of Environmental Chemical Engineering, vol. 13, no. 2, p. 115646, Jan. 2025, doi: https://doi.org/10.1016/j.jece.2025.115646.
[4] N. Poonia et al., "Iron oxide nanoparticles: a versatile nanoplatform for the treatment and diagnosis of ovarian cancer," Therapeutic Delivery, vol. 16, no. 4, pp. 379–392, Dec. 2024, doi: https://doi.org/10.1080/20415990.2024.2442301.
[5] A. N. Cheema, Iqra Muneer, N. Maham, Farhat Yasmeen, and D. Ali, "Impact of niobium doping on photocatalytic degradation efficiency of iron oxide nanoparticles for methylene blue dye under UV and sunlight," Materials Science and Engineering B, vol. 312, pp. 117878–117878, Dec. 2024, doi: https://doi.org/10.1016/j.mseb.2024.117878.
[6] T. Devender Reddy, G. Padmasree, S. Yelipeddy, P. Yadagiri Reddy, and C. Gopal Reddy, "Magnetic and 57Fe Mössbauer studies of praseodymium (Pr) substituted yttrium iron oxide (YFeO3) materials prepared by sol-gel technique," Bulletin of Materials Science, vol. 48, no. 2, Apr. 2025, doi: https://doi.org/10.1007/s12034-025-03417-2.
[7] H. Yang et al., "Magnetic iron oxide nanoparticles: An emerging threat for the environment and human health," Journal of Environmental Sciences, vol. 152, pp. 188–202, May 2024, doi: https://doi.org/10.1016/j.jes.2024.04.045.
[8] A. Ashwini, G. Kaladevi, M. George, and S. C. B. Gopinath, "Alloyed CeCaxFe1-xO3-δ: A calcium doped cerium iron oxide nanomaterial for photo-Fenton degradation," Journal of Crystal Growth, pp. 128177–128177, Apr. 2025, doi: https://doi.org/10.1016/j.jcrysgro.2025.128177.
[9] B. Arunkumar and M. Jothibas, "Exploring different dopant materials in conjunction with iron oxide and analyzing their characterization and magnetic properties," Chemical Physics, vol. 588, p. 112477, Jan. 2025, doi: https://doi.org/10.1016/j.chemphys.2024.112477.
[10] R. Kumar, R. K. Nekouei, and V. Sahajwalla, "In-situ carbon-coated iron oxide (ISCC-Fe3O4) as an efficient electrode material for supercapacitor applications," Ceramics International, Jan. 2025, doi: https://doi.org/10.1016/j.ceramint.2025.01.071.
[11] Y. Wu, C. Wang, L. Wang, and C. Hou, "Recent Advances in Iron Oxide-Based Heterojunction Photo-Fenton Catalysts for the Elimination of Organic Pollutants," Catalysts, vol. 15, no. 4, pp. 391–391, Apr. 2025, doi: https://doi.org/10.3390/catal15040391.
[12] A. Pandey, S. K. Saini, R. K. Singh, and T. Mohanty, "Power dependent tunable optical nonlinearity in Iron oxide/Borophene core-shell nanoparticles under ultrashort laser excitation," Optics & Laser Technology, vol. 181, pp. 111761–111761, Sep. 2024, doi: https://doi.org/10.1016/j.optlastec.2024.111761.
[13] M. Moradi, M. Rouhani, M. Hekmati, H. Veisi, and D. Esmaeli, "Green synthesis of gold nanoparticles supported over the Myrtus communis L extract modified magnetic iron oxide as a novel antibacterial agent," Results in Chemistry, vol. 15, p. 102323, May 2025, doi: https://doi.org/10.1016/j.rechem.2025.102323.
[14] F. Dumitrache et al., "Experimental Study Regarding the Synthesis of Iron Oxide Nanoparticles by Laser Pyrolysis Using Ethanol as Sensitizer; Morpho-Structural Alterations Using Thermal Treatments on the Synthesized Nanoparticles," Coatings, vol. 15, no. 2, p. 234, Feb. 2025, doi: https://doi.org/10.3390/coatings15020234.
[15] T. G. Khonina et al., "Iron(III) Monoglycerolate: A Potential Hemostatic Agent for Topical Application," Current Bioactive Compounds, vol. 21, no. 3, May 2024, doi: https://doi.org/10.2174/0115734072295011240425080837.
[16] C. Li, S. He, H. Mo, X. Xu, P. Yang, and M. Liu, "Recent developments of iron oxide-based photocatalysts in water treatment technology: a review," Environmental Science: Water Research & Technology, vol. 11, no. 6, pp. 1369–1385, 2025, doi: https://doi.org/10.1039/d5ew00021a.
[17] R. H. Pham, Ireshika Wickramasuriya, M. Wright, V. Taufour, S. Kamali, and B. S. Guiton, "Lab-Scale Synthesis of Hollow Iron Oxide Nanocapsules with a Metastable Magnetic Maghemite Phase," ACS Applied Nano Materials, Mar. 2025, doi: https://doi.org/10.1021/acsanm.4c06535.
[18] Asma Arfaoui and Ammar Mhamdi, "Synthesis and Characterization of SnO2/α-Fe2O3, In2O3/α-Fe2O3, and ZnO/α-Fe2O3 Thin Films: Photocatalytic and Antibacterial Applications," Surfaces, vol. 8, no. 1, pp. 8–8, Jan. 2025, doi: https://doi.org/10.3390/surfaces8010008.
[19] T. Yang and W. Yan, "Strategies for enhancing the antibacterial efficacy of lysozyme and the resulting outcome," International Journal of Biological Macromolecules, vol. 310, p. 143137, Apr. 2025, doi: https://doi.org/10.1016/j.ijbiomac.2025.143137.
[20] X. Wei et al., "Bone Immune Microenvironment-Modulating Naringin Carbon Dot Complex Hydrogel with ROS-Scavenging and Antibacterial Properties for Enhanced Bone Repair," ACS Applied Materials & Interfaces, May 2025, doi: https://doi.org/10.1021/acsami.5c07627.

*Corresponding author
Taghreed nesaef Jasem,
Ministry of Education, Baghdad, Iraq Republic of Iraq, Ministry of Education Directorate of Education – Al-Karkh /1, Baghdad, Iraq
e-mail: daghreedjasem@gmail.com